Supporting Information

Murphy et al. 10.1073/pnas.0909299107

SI Results

The amino-triazole motif is predicted to form specific interactions between the 1,2-nitrogens of the triazole ring and the main-chain nitrogen of D594 (B-RAF) or D259 (PDGFRβ) as well as between the 1N*H* and N*H*-phenyl amines and E501(B-RAF) and E66 (PDGFRβ) (Fig. 1*A*). The trifluoromethyl group on the terminal phenyl ring is predicted to bind tightly to the hydrophobic pocket located between the αC and αE helices and the N-terminal regions of the DFG motif and catalytic loop in both B-RAF and PDGFRβ, thereby impacting the location of the F595 (B-RAF) or F260 (PDGFRβ) phenyl ring and stabilizing the DFG-out conformation (Fig. 1*A*). Additionally, the methylthiol present on **6** is predicted to interact with the W530 side chain in B-RAF and help guide the binding of the small molecule within the allosteric site (Fig. 1*A*), and this substituent is important for inhibition of RAF signaling within endothelial cells. Similarly, substitution of 4-Cl on the terminal phenyl ring prevents PDGFRβ activity and, from comparative structural analysis of EGFR kinase, 4-Cl is predicted to clash with the activation loop of PDGFRβ (Fig. S1*B*).

Structure–Activity Relationships from Cell-Based Screening. A comparison of nine representative compounds (**3**–**11**) demonstrates several key sites for cell-based phosphorylation of both PDGFRβ and MEK (Fig. 1*D*). Starting with a linear heterocyclic scaffold, we determined that four substituents contributed to both activities as predicted by molecular modeling (Fig. 1*A* and Fig. S1*B*). These four positions are designated X_1, X_2, Y, or Z in the general inhibitor structure (Fig. 1*D*). The X_1 substituent is predicted to be critical for proper orientation of the pyrimidine ring, which greatly enhances inhibition of p-MEK in endothelial cells. Compound **3**, which is unsubstituted at the X_1 position, is a potent inhibitor of p-PDGFRβ but does not suppress p-MEK, suggesting that substitution at X_1 is important for tuning the kinase profile. Addition of an amino group to **3** at X_1 yields **4**, which does not produce a change in cell-based inhibition. Substitution of **4** with 4-chloro in the Z position on the phenyl gives **5**, which abolishes the inhibition of p-PDGFRβ in vascular smooth muscle cells (VSMCs) but enables the inhibition of p-MEK in human umbilical vein endothelial cells (HUVECs). Importantly, addition of 2-methylthio at X_1 to compound **3** produces **6**, which demonstrates dual inhibition of PDGFRβ autophosphorylation and MEK phosphorylation. The methylthiol group is predicted to interact with W530 in B-RAF and orient **6** within the allosteric site of B-RAF, whereas the corresponding Y309 in PDGFRβ is not predicted to provide the same interaction (Fig. 1*A*). Removal of the amine at X_2 from **6** on the pyrimidine produces **7** and reduces its PDGFRβ inhibitory activity, demonstrating the importance of the X_2 substituent on the pyrimidine ring. Addition of 4-chloro at the Z position in **6** gives compound **8**, which produces similar results to **5**, signifying that the 4-chloro substitution abolishes the inhibition of p-PDGFRβ but does not affect p-MEK. This is expected, as the 4-Cl group is predicted to clash with a loop in close proximity based on using the inactive EGFR conformation as a template, because this loop is not resolved in the B-RAF or PDGFRβ structures (Fig. S1*B*). Substituting methoxy (**9**) for amine (**4**) in X_2 enables dual inhibition as observed with **6**. Additionally, in the case of **10** and **11**, where the triazole ring in **4** and **6**, respectively, is substituted with an oxadiazole (position Y), a reduction in p-MEK inhibition is observed and p-PDGFRβ is not inhibited. This is likely due to the replacement of a hydrogen-bond donor with a hydrogen-bond acceptor and an overall change in the bond angle of the oxadiazole compared to the triazole. The trifluoromethyl group on the terminal phenyl ring is predicted to be critical for binding to the hydrophobic pocket, which is available for binding when F of the DFG motif is displaced in the PDGFRβ and B-RAF inactive conformation. The SAR demonstrates that a 4-chloro in the Z position eliminates PDGFRβ inhibition, a triazole ring (amine in position Y) is favored for inhibiting both p-PDGFRβ and p-MEK, and substitution of the pyrimidine ring at X_1 and X_2 greatly affects the inhibition of p-PDGFRβ and p-MEK. These observations are supported by the predicted binding mode of **6** in both the PDGFRβ and B-RAF inactive conformations (Fig. 1*A*), and identify substituents which enable fine-tuning of the kinase profile.

Compound 6 Inhibits RAF and PDGFR Signaling but Does Not Influence a Variety of Other Cellular Targets. Compound **6** directly impacts PDGFRβ autophosphorylation in response to PDGF-BB and inhibits MAPK signaling in response to bFGF or VEGF. To study this further, lysates of bFGF- or VEGF-stimulated endothelial cells (ECs) treated in the presence or absence of **6** were analyzed for the activation of a variety of signaling cascades. Whereas **6** blocked p-MEK and p-ERK in response to either growth factor, it did not suppress p-Akt, suggesting that **6** inhibits RAF because it impacts the MAPK pathway downstream of Ras but upstream of MEK. We also observed no effect on integrin-mediated signaling to FAK or Src and saw no impact on PKC (Table S4). Importantly, **6** inhibited bFGF- or VEGF-mediated phosphorylation of MEK on S217/S221 but not on S298 (Fig. 1*C*). MEK S217/S221 is the well-known RAF phosphorylation site important for MEK activation, whereas MEK S298 has been shown to be phosphorylated by p21-activated kinase (PAK), which can lead to MEK activation. Therefore, **6** does not directly inhibit PAK activity.

Materials and Methods

Biological Assays and in Vivo Models. ***Computational Docking Studies.*** The x-ray crystal structure of B-RAF with BAY43-9006 (sorafenib) was selected for docking studies because it contained the DFG motif of the activation loop in a desirable inactive state (i.e., DFG-out). Moreover, this inactive state is stabilized by a small molecule, and as a result provides an appropriate ligand-induced conformation for docking with **6**. The Docking module of InsightII (Accelrys) was used to perform ligand docking studies with the previously reported cocrystal structure of B-RAF with BAY 43-9006 (sorafenib). This inactive conformation was chosen because stabilizing the DFG-out structure is important for the type II kinase inhibition mode. As a measure of docking accuracy, the ligand from the crystal structure, BAY43-9006, was removed and docking from a 2D structure of this molecule was performed and qualitatively interpreted. The homology model of the PDGFRβ kinase module was created based on the crystal structure of VEGFR2 (PDB ID code 1Y6B). VEGFR2 and PDGFRβ share 46% sequence identity within the kinase domain. Homology modeling was performed using the Homology module of the InsightII program (Accelrys). The model underwent 10,000 iterations of molecular mechanics minimization with the program Discover (Accelrys) after its construction. The docking of **6** to this structure was performed as described above.

Immunoprecipitation and Immunoblotting. Following stimulation with bFGF, VEGFA, or PDGF-BB, cells were washed once with ice-cold PBS and lysed in RIPA buffer. For the PDGFRβ autophosphorylation assay in VSMCs, 500 μg of protein from lysates was incubated with 3 μg of anti-PDGFRβ (sc-432; Santa Cruz Biotechnology) for 1 h at 4 °C and subsequently tumbled over-

night with protein A/G beads (Pierce) for immunoprecipitation. For the MAPK assay in HUVECs, standard SDS/PAGE and immunoblotting were performed using antibodies to phospho-MEK S217/S221, phospho-MEK S298, phospho-ERK T202/Y204, phospho-C-RAF S259 and S338 (all from Cell Signaling), and MEK1, ERK2, and C-RAF (all from Santa Cruz Biotechnology). For the PDGFRβ autophosphorylation assay, antibodies to PDGFRβ (sc-339; Santa Cruz Biotechnology) and HRP-conjugated PY-20 (sc-508; Santa Cruz Biotechnology) were used to detect total PDGFRβ and phospho-tyrosine levels, respectively. HRP-conjugated primary or secondary Abs were detected with SuperSignal ECL (Pierce).

Cell Viability Assays. For XTT assays, cells were grown in 96-well plates overnight and all assays were conducted in growth medium with full serum and additives. Compounds were serially diluted in DMSO and then further diluted into the medium to give the appropriate concentration while minimizing precipitation associated with serial diluting in medium alone. Inhibitors were added for 72 h and cell viability was quantified at 450 nm after the addition of 1 mg/mL XTT solution (Sigma-Aldrich) in phenol-red free DMEM medium containing phenoxymethosulfate (Sigma-Aldrich). Dose–response curves were plotted using GraphPad Prism software and EC_{50}s were calculated using this program.

Stellate Cell/Endothelial Cell Coculture Assay for Endothelial Tube Formation. Early-passage ($P < 5$) human telomerase reverse transcriptase-hepatic stellate cells (stellate cells), a generous gift from Dr. David Brenner (La Jolla, CA), were labeled with 10 μg/mL red fluorescent dye DiIC(3) (BD Biosciences) for 2 h at 37 °C. The stellate cells were washed in PBS and mixed with early-passage HUVECs ($P < 5$) at a ratio of 1:4 and mixed into a 3.75 mg/mL type 1 rat-tail collagen matrix (BD Biosciences) in M-199 media. Thirty microliters of this mixture was seeded onto each well of a half-area 96-well plate (Corning). The collagen was allowed to polymerize for 30 min at 37 °C and 100 μL of complete EBM-2 media was added to each well. Various inhibitors were serially diluted in DMSO and subsequently added to duplicate wells 6 h post-cell-seeding. The endothelial tubes were stained at 24 h by adding 2 μL FITC-labeled *Ulex europaeus* lectin (Vector Labs) per well. The endothelial tubes and stellate cells were imaged at 48 h with a 10× objective on a confocal microscope. Images were collected across five fields per well. Tube lengths were measured using MetaMorph software for each tube for all 10 microscopic fields from the duplicate wells. The % pericyte-covered tube length was calculated from the ratio of tube length sums for the tubes with and without pericyte contact.

Mouse Matrigel Model of Angiogenesis. Female Nu/Nu mice were implanted with growth-factor-depleted Matrigel (BD Biosciences) in the flank containing either PBS or 200 ng of bFGF (Peprotech). The following morning, mice were treated with **6**, control compound, or vehicle (10% HS-15 in 3.3% dextrose) by i.p. injection on a bid (twice daily) dosing schedule. Five days after Matrigel implantation, mice were tail-vein-injected with FITC-lectin and plugs were harvested and imaged by confocal microscopy and quantified after homogenization in ice-cold PBS using a fluorescent microplate reader (Tecan Systems).

For immunohistochemistry, mice were implanted with Matrigel plugs with the same dosing schedule described above. On day 5, the plugs were excised and 5-μm sections were generated. The sections were fixed according to the Apoptag protocol in which immunostaining was added during the TUNEL-staining process as well as TO-PRO-3 (Invitrogen) for a nuclear counterstain. The sections were labeled with anti-phospho-ERK T202/Y204 (Cell Signaling) and an endothelial cell mix consisting of anti-CD31, anti-Flk, anti-VE-cadherin (all from BD Biosciences), and anti-endoglin (Millipore). Primary antibodies were added at 1:100 dilutions and the corresponding secondary anti-rat Ab was added at a 1:250 dilution. The tricolor images were generated with confocal microscopy.

Orthotopic Pancreatic Carcinoma Model. Orthotopic human pancreatic cancer xenografts from the pancreatic cancer cell line XPA-1-RFP were established in nude mice by surgical orthotopic implantation (SOI). Briefly, s.c. XPA-1-RFP tumors in the exponential growth phase were harvested and sectioned into 1-mm^3 pieces in serum-free RPMI medium. Mice were anesthetized using 50% ketamine, 38% xylazine, and 12% agepromazine maleate injected intramuscularly at a dose of 2 μL/g, and their abdominal wall was sterilized with alcohol. A small incision was then made in the right pararectal line through the skin and peritoneum. The body of the pancreas was exposed and a 1-mm^3 tumor fragment was sutured to the pancreas using a single 8-0 nylon surgical suture (Davis-Geck). The pancreas was then returned to the abdomen and the peritoneum and skin were closed in two layers using 6-0 vicryl surgical sutures.

At day 3 after SOI, the animals began treatment with twice-daily i.p. injections of either compound, **6** (50 mg/kg dose in 200-μL total volume) or vehicle control, at 12-h intervals. The animals were weighed and imaged every 3 days starting at day 3 post-SOI using the Olympus OV100 Small Animal Imaging System (Olympus), containing an MT-20 light source (Olympus Biosystems) and DP70 CCD camera (Olympus). All images were processed for contrast and brightness with the use of Photoshop element 4. All measurements were made using ImageJ software. At day 12 post-SOI the animals were killed and their tumors were excised, weighed, and measured in three dimensions to calculate tumor volume. The tumor volume was calculated with the formula: volume = height × width × length × 0.52. Ex vivo tumors were then compressed and imaged using the OV100 system. The total vessel length for each tumor was measured using ImageJ software and converted to vessel density by dividing total tumor vessel length by tumor volume.

Orthotopic Renal Cell Carcinoma Model. Male Nu/Nu mice were anesthetized with an i.p. injection of 50 mg/kg ketamine and 10 mg/kg medetomidine. A small incision was made along the left flank of the mice and the kidney was exposed. A 27-gauge insulin syringe was used for orthotopic injection of the SN12C-RFP cells. One million tumor cells in 20 μL of a 1:1 PBS:Matrigel mixture were injected into the lower pole of the kidney just below the renal subcapsule. The needle was removed after a visible blister formed, and leakage of the tumor cell suspension was minimal. The abdominal wall was closed by suturing the peritoneal membrane followed by stapling the dermal layer. Animals which formed visible blisters upon injection in the subcapsule with minimal leakage were used for the efficacy study. Male Nu/Nu mice with orthotopic injections of the SN12C-RFP cells were imaged using the Olympus OV100 Small Animal Imaging System and grouped on day 7 based on weight and imaging results. The mice were dosed orally at 100 mg/kg daily with **6** in 10% HS-15 and 3.3% dextrose. At the end of the study, the kidney tumors were imaged with the OV-100 system for RFP expression and then the kidneys were resected and weighed. The difference in weight between the tumor-bearing kidney and the normal kidney was reported.

Synthesis and Characterization of Compounds. ***General Synthetic Methods.*** Unless otherwise noted, materials were obtained from commercial suppliers and used without purification. Removal of solvent in vacuo refers to distillation using a Büchi R-200 rotary evaporator and a Welch 2025 vacuum pump.

All microwave irradiation experiments were carried out in an Initiator (Biotage) microwave apparatus in the standard configuration including the proprietary Biotage software. The reactions were carried out in 5-mL Emrys microwave vials. After the irradiation period, the reaction vessel was cooled rapidly (1–2 min) to ambient temperature by gas jet cooling.

^1H and ^{13}C NMR spectra were recorded on a Bruker AMX-II (500 MHz) spectrometer. Proton resonances are reported in parts

per million (ppm) downfield from tetramethylsilane (TMS). ^{1}H NMR data are reported as multiplicity (s, singlet; d, doublet; t, triplet; q, quartet; dd, doublet of doublets; dt, doublet of triplets; br, s broad singlet), coupling constant in Hertz and number of protons. The ^{1}H and ^{13}C NMR spectra were obtained in DMSO-d_6 (99.96 DMSO-d_6 with 0.03 vol/vol TMS). The ^{1}H NMR spectra for 1,2,4-triazoles were recorded at 80 °C to induce the rapid exchange of the N-proton of the triazole ring. Due to the intermediate-to-slow exchange of the N-proton of the triazole ring at room temperature, the broadening of the peaks is observed in both ^{1}H and ^{13}C NMR spectra recorded at ambient temperature. All data were processed with Xwin-NMR software (Bruker).

High-pressure liquid chromatography was done using a Gilson Unipoint 215 liquid handler with a 151 UV/vis detector and Waters PrepLC 40-mm module with SymmetryShield RP18 7-μm 40 × 100 mm PrepPak cartridges. Purification of compounds by high-pressure liquid chromatography was performed at a 40 mL/min flow rate with a gradient from 10% of solvent B (acetonitrile with 0.1% TFA) in solvent A (water with 0.1% TFA) to 100% solvent B in 25 min, followed by 5 min elution with 100% solvent B.

Analytical TLC was performed on commercial silica plates (EMD Chemicals; silica gel 60 F254, 0.25-mm thickness). Compounds were visualized by UV light (254 nm). Flash chromatography was performed either by CombiFlash (Companion; Teledyne ISCO) or using silica gel (ICN silica 32-63 D 60 Å).

A Waters 2795 LC/MS with Micromass ZQ and 2996 PDA detector were used to monitor the progress of reactions and check the purity of products. Mass spectra were obtained in electrospray ionization (ESI) positive mode.

Accurate masses were measured by ESI time-of-flight (TOF) reflectron experiments performed on an Agilent ESI-TOF mass spectrometer. Samples were electrosprayed into the TOF reflectron analyzer at an ESI voltage of 4000 V and a flow rate of 200 μL/min.

Synthesis of Compounds 3–9

Scheme 1.

S-Methyl N-[3-(Trifluoromethyl)phenyl]isothiourea Hydroiodide (1a). To a solution of 3-trifluoromethyl-phenylthiourea (5.53 g, 25.1 mmol) in anhydrous MeOH (100 mL) was added methyl iodide (3.92 g, 27.6 mmol) via a syringe. The reaction mixture was refluxed for 12 h. Then it was cooled down to ambient temperature and solvent was removed in vacuo to give a light-yellow oil (9.09 g), which was taken to the next step without further purification.

4-(5-{[3-(Trifluoromethyl)phenyl]amino}-4*H*-1,2,4-triazol-3-yl)-phenol (2a). 4-Hydroxybenzoic acid hydrazide (3.82 g, 25.1 mmol) and **1a** (9.1 g, 25.1 mmol) were suspended in anhydrous pyridine (80 mL). The reaction mixture was heated at reflux under argon atmosphere for 18 h. Then it was cooled down to ambient temperature and pyridine was removed in vacuo. The resulting solid was redissolved in a minimum amount of ethyl acetate and passed through a short pad of silica gel. The silica gel was washed with EtOAc. Combined organic solutions were concentrated in vacuo with ca 15 g of silica gel. The loaded silica gel was further purified by the ISCO system [80-g Redi*Sep* column (Teledyne ISCO), solid method, 0–50% EtOAc gradient in hexanes, 45-min method]. Fractions containing the product were combined and concentrated in vacuo to give the title product as a white solid (3.83 g, 48%).

4-{5-[(4-Chloro-3-(trifluoromethyl)phenyl)amino]-4*H*-1,2,4-triazol-3-yl} phenol (2b). 4-Hydroxybenzoic acid hydrazide (4.07 g, 26.8 mmol)

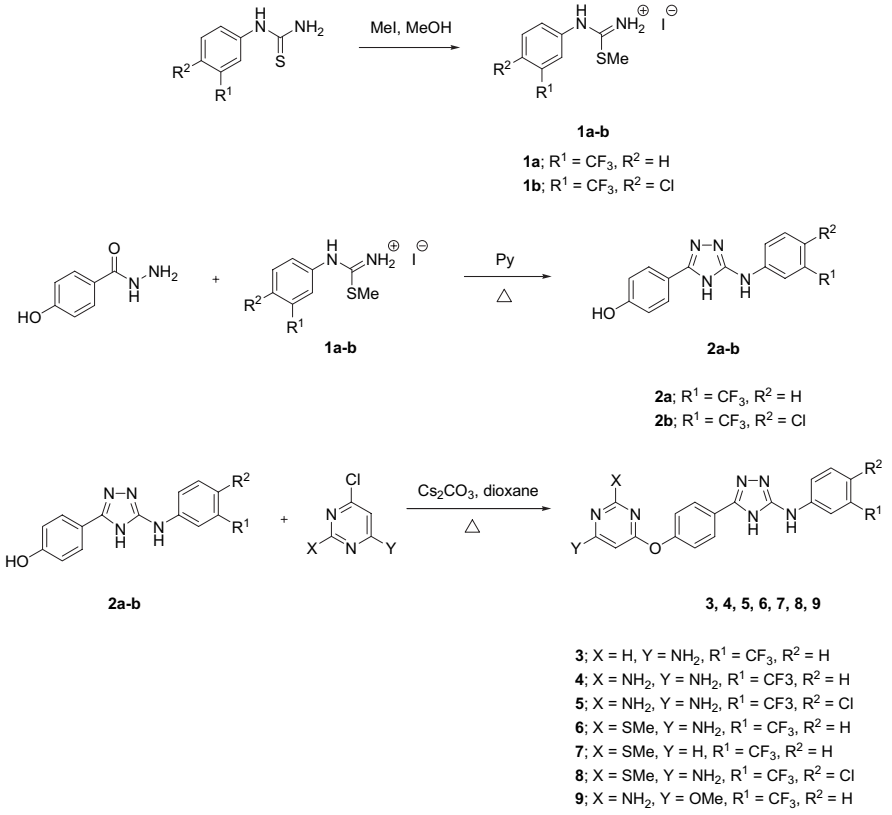

and S-methyl N-(4-chloro-3-(trifluoromethyl)phenyl)isothiourea hydroiodide (10.62 g, 26.8 mmol) were suspended in anhydrous pyridine (80 mL). The reaction mixture was refluxed under argon atmosphere for 5 h. Then it was cooled down to ambient temperature and pyridine was removed in vacuo. The residue was redissolved in EtOAc (100 mL) and the solution was concentrated in vacuo with ca 15 g of silica gel. The loaded silica gel was further purified by the ISCO system [80-g Redi*Sep* column (Teledyne ISCO), solid method, 10–50% EtOAc gradient in hexanes, 45-min method]. Fractions containing the product were combined and concentrated in vacuo to give a pale-yellow solid. The solid was recrystallized from ca 30 mL of MeOH, collected by centrifugation, washed with Et_2O (3 × 40 mL), and dried in vacuo to give the title product as a white fluffy solid (3.42 g, 36%).

6-[4-(5-{[3-(Trifluoromethyl)phenyl]amino}-4*H*-[1,2,4]-triazol-3-yl)-phenoxy]-pyrimidin-4-amine (3). A 5-mL Emrys microwave vial was charged with **2a** (100 mg, 0.31 mmol), 4-amino-6-chloropyrimidine (49 mg, 0.37 mmol), cesium carbonate (102 mg, 0.31 mmol), and anhydrous dioxane (5 mL). The reaction mixture was stirred at ambient temperature for 10 min, then sealed and irradiated in a microwave (Initiator; Biotage) at 200 °C for 5 min. After cooling to ambient temperature, the reaction mixture was concentrated in vacuo. The residue was redissolved in DMF (3 mL), filtered through a 0.2-μm syringe filter, and purified by reverse-phase preparative HPLC. Fractions containing the product were combined and poured into EtOAc (50 mL). The resulting mixture was washed with saturated aqueous $NaHCO_3$ (2 × 50 mL) and brine (2 × 50 mL), dried over anhydrous Na_2SO_4, and filtered. Solvent was removed in vacuo to give the title product as a white solid (77 mg, 60%).

^{1}H NMR (500 MHz, DMSO-d_6, 80 °C): δ 5.88 (s, ^{1}H), 6.60 (s, 2H), 7.12 (d, J = 7.7 Hz, ^{1}H), 7.27 (d, J = 8.7 Hz, 2H), 7.45 (t, J = 8.0 Hz, ^{1}H), 7.79 (dd, J = 8.3, 1.7 Hz, ^{1}H), 8.00 (d, J = 8.8 Hz, 2H), 8.05 (s, ^{1}H), 8.10 (d, J = 0.7 Hz, ^{1}H), 9.38 (s, ^{1}H), 13.44 (br s, ^{1}H). ^{13}C NMR (125 MHz, DMSO-d_6): δ 86.9, 111.5, 115.0, 119.3, 122.2, 124.0, 124.5 (q, $J_{C\text{-}F}$ = 270.3 Hz, CF_3), 127.4, 129.6 (q, J = 30.9 Hz), 129.7, 142.7, 151.9, 154.3, 158.2, 160.2, 166.1, 168.8.

HRMS (ESI-TOF): calcd for $C_{19}H_{14}F_3N_7O$ $[M+H]^+$ 414.1285, found 414.1285. Anal: Calcd for $C_{19}H_{14}F_3N_7O$ x $0.2H_2O$: C, 54.73; H, 3.48; N, 23.51. Found: C, 54.81; H, 3.25; N, 23.26.

6-{4-(5-{[3-(Trifluoromethyl)phenyl]amino}-4*H*-[1,2,4]-triazol-3-yl) phenoxy}-pyrimidin-2,4-diamine (4). The compound was prepared according to the same procedure as in the synthesis of **6** exemplified in Scheme 1.

^{1}H NMR (500 MHz, DMSO-d_6): δ 5.25 (s, ^{1}H), 5.66 (s, 2H), 6.00 (s, 2H), 7.13 (d, J = 7.4 Hz, ^{1}H), 7.23 (d, J = 8.5 Hz, 2H), 7.46 (t, J = 8.0 Hz, ^{1}H), 7.80 (d, J = 8.2 Hz, ^{1}H), 7.98 (d, J = 8.6 Hz, 2H), 8.06 (s, ^{1}H), 9.33 (br s, ^{1}H), 13.42 (br s ^{1}H).

HRMS (ESI-TOF): calcd for $C_{19}H_{16}F_3N_8O$ $[M+H]^+$ 429.1399, found 429.1387.

6-{4-[5-(4-Chloro-3-trifluoromethyl-phenylamino)-4*H*-[1,2,4]-triazol-3-yl]phenoxy}-pyrimidin-2,4-diamine (5). The compound was prepared according to the same procedure as in the synthesis of **6** exemplified in Scheme 1.

^{1}H NMR (500 MHz, DMSO-d_6): δ 5.26 (s, ^{1}H), 5.66 (s, 2H), 6.00 (s, 2H), 7.24 (d, J = 8.6 Hz, 2H), 7.52 (d, J = 8.8 Hz, ^{1}H), 7.81 (dd, J = 8.8, 2.4 Hz, ^{1}H), 7.97 (d, J = 8.7 Hz, 2H), 8.21 (d, J = 2.6 Hz, ^{1}H), 9.48 (br s, ^{1}H), 13.51 (br s ^{1}H).

HRMS (ESI-TOF): calcd for $C_{19}H_{15}ClF_3N_8O$ $[M+H]^+$ 463.1009, found 463.1002.

2-(Methylthio)-6-[4-(3-{[3-(trifluoromethyl)phenyl]amino}-4*H*-1,2,4-triazol-5-yl)-phenoxy]pyrimidin-4-amine (6). A 5-mL Emrys microwave vial was charged with **2a** (100 mg, 0.31 mmol), 4-amino-6-chloro-2-(methylthio)pyrimidine (60 mg, 0.34 mmol), cesium carbonate (102 mg, 0.31 mmol), and anhydrous dioxane (5 mL). The reaction mixture was stirred at ambient temperature for 10 min, then sealed and irradiated in a microwave (Initiator; Biotage) at 200 °C for 20 min. After cooling to ambient temperature, the reaction mixture was concentrated in vacuo. The residue was redissolved in DMF (3 mL), filtered through a 0.2-μm syringe filter, and purified by reverse-phase preparative HPLC in a CH_3CN/H_2O system containing 0.1% TFA. Fractions containing the product were combined and poured into EtOAc (50 mL). The resulting mixture was washed with saturated aqueous $NaHCO_3$ (2 × 50 mL) and brine (2 × 50 mL), dried over anhydrous Na_2SO_4, and filtered. Solvent was removed in vacuo to give the title product as a white solid (40 mg, 28%).

^{1}H NMR (500 MHz, DMSO-d_6, 80 °C): δ 2.32 (s, 3H), 5.58 (s, ^{1}H), 6.65 (s, 2H), 7.12 (d, J = 7.7 Hz, ^{1}H), 7.29 (d, J = 8.7 Hz, 2H), 7.45 (t, J = 8.0 Hz, ^{1}H), 7.80 (dd, J = 8.2, 1.9 Hz, ^{1}H), 8.01 (d, J = 8.7 Hz, 2H), 8.05 (s, ^{1}H), 9.39 (s, ^{1}H), 13.45 (br s, ^{1}H). ^{13}C NMR (125 MHz, DMSO-d_6): δ 13.1, 82.7, 111.6, 115.2, 119.5, 122.1, 124.2, 124.4 (q, $J_{C\text{-}F}$ = 270.5 Hz, CF_3), 127.3, 129.6 (q, J = 30.8 Hz), 129.7, 142.6, 152.0, 153.9, 160.2, 165.7, 168.6, 170.4.

HRMS (ESI-TOF): calcd for $C_{20}H_{16}F_3N_7OS$ $[M+H]^+$ 460.1162, found 460.1166. Anal. Calcd for $C_{20}H_{16}F_3N_7OS$ x $2H_2O$: C, 48.48; H, 4.07; N, 19.79; S, 6.74. Found: C, 48.42; H, 3.90; N, 19.54; S, 6.47.

5-(4-{[2-(Methylthio)pyrimidin-4-yl]oxy}phenyl)-*N*-[3-(trifluoromethyl) phenyl]-4*H*-1,2,4-triazol-3-amine (7). A 5-mL Emrys vial was charged with **2a** (320 mg, 1.00 mmol) and anhydrous dioxane (5 mL). The vial was placed in a heating block at 100 °C. Solid cesium carbonate was added (326 mg, 1.00 mmol), followed after 10 min by 4-chloro-2-methylthiopyrimidine (177 mg, 1.10 mmol). The vial was then sealed and the reaction mixture was left to stir at 120 °C for 18 h. After cooling to ambient temperature, the reaction mixture was concentrated in vacuo. The residue was redissolved in DMF (4 mL), filtered through a 0.2-μm syringe filter, and purified by reverse-phase preparative HPLC. Fractions containing the product were combined and poured into EtOAc (50 mL). The resulting mixture was washed with saturated aqueous $NaHCO_3$ (2 × 50 mL) and brine (2 × 50 mL), dried over anhydrous Na_2SO_4, and filtered. Solvent was removed in vacuo to give the title product as a white solid (159 mg, 36%).

^{1}H NMR (500 MHz, DMSO-d_6, 80 °C): δ 2.38 (s, 3H), 6.78 (d, J = 5.8 Hz, ^{1}H), 7.13 (d, J = 7.6 Hz, ^{1}H), 7.37 (d, J = 8.6 Hz, 2H), 7.46 (t, J = 8.0 Hz, ^{1}H), 7.82 (dd, J = 8.3, 1.7 Hz, ^{1}H), 8.06–8.09 (m, 3H), 8.50 (d, J = 5.8 Hz, ^{1}H), 9.47 (s, ^{1}H), 13.56 (br s, ^{1}H). ^{13}C NMR (125 MHz, DMSO-d_6): δ 13.4, 103.6, 111.6, 115.1, 119.4, 122.3, 124.4 (q, $J_{C\text{-}F}$ = 270.6 Hz, CF_3), 124.8, 127.4, 129.6 (q, J = 30.9 Hz), 129.7, 142.6, 151.7, 152.9, 159.6, 160.2, 168.1, 171.4.

HRMS (ESI-TOF): calcd for $C_{20}H_{15}F_3N_6OS$ $[M+H]^+$ 445.1053, found 445.1042. Anal. Calcd for $C_{20}H_{15}F_3N_6OS$ x $2.3H_2O$: C, 49.44; H, 4.07; N, 17.30; S, 6.60. Found: C, 49.34; H, 3.77, N, 17.14, S, 6.67.

2-(Methylthio)-6-[4-(5-{[4-chloro-3-(trifluoromethyl)phenyl]amino}-4*H*-[1,2,4]-triazol-3-yl)phenoxy]-pyrimidin-4-amine (8). The compound was prepared according to the same procedure as in the synthesis of **6** exemplified in Scheme 1.

^{1}H NMR (500 MHz, DMSO-d_6): δ 2.33 (s, 3H), 5.60 (s, ^{1}H), 6.64 (s, 2H), 7.30 (d, J = 8.7 Hz, 2H), 7.53 (d, J = 8.8 Hz, ^{1}H), 7.82 (dd, J = 8.8, 2.6 Hz, ^{1}H), 8.01 (d, J = 8.7 Hz, 2H), 8.21 (d, J = 2.6 Hz, ^{1}H), 9.53 (br s, ^{1}H), 13.40 (br s ^{1}H).

HRMS (ESI-TOF): calcd for $C_{20}H_{16}ClF_3N_7OS$ $[M+H]^+$ 494.0778, found 494.0766.

4-Methoxy-6-[4-(5-{[3-(trifluoromethyl)phenyl]amino}-4*H*-[1,2,4]-triazol-3-yl)phenoxy]pyrimidin-2-amine (9). The compound was prepared according to the same procedure as in the synthesis of **6** exemplified in Scheme 1.

^{1}H NMR (500 MHz, DMSO-d_6): δ 3.01 (s, 3H), 5.51 (s, ^{1}H), 6.35 (s, 2H), 7.13 (d, J = 7.4 Hz, ^{1}H), 7.28 (d, J = 8.5 Hz, 2H), 7.46 (t, J = 7.9 Hz, ^{1}H), 7.80 (d, J = 8.7 Hz, ^{1}H), 8.00 (d, J = 8.7 Hz, 2H), 8.06 (s, ^{1}H), 9.37 (br s, ^{1}H), 13.46 (br s ^{1}H).

HRMS (ESI-TOF): calcd for $C_{20}H_{17}F_3N_7O_2$ $[M+H]^+$ 444.1396, found 444.1386.

Synthesis of Compounds 10 and 11

Scheme 2.

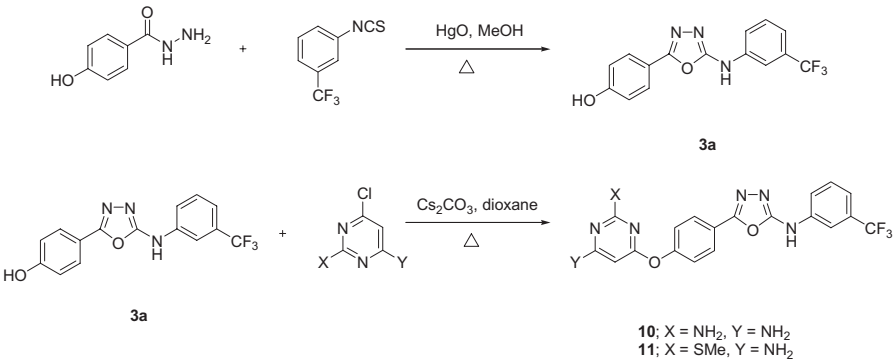

4-(5-{[3-(Trifluoromethyl)phenyl]amino}-1,3,4-oxadiazol-2-yl)phenol (3a). To a suspension of Hg(II)O in anhydrous MeOH (70 mL) was added 4-hydroxybenzoic acid hydrazide (3.74 g, 24.6 mmol), followed by 3-trifluorophenylisothiocyanate (5.0 g, 24.6 mmol). The reaction mixture was brought to reflux and refluxed for 2 h. Then it was cooled down to ambient temperature and filtered through a short pad of celite. The celite pad was washed with MeOH. Organic solutions were combined and concentrated in vacuo. The residue was recrystallized from ca 100 mL of EtOAc. The formed crystalline material was filtered, washed with EtOAc (10 mL), and dried in vacuo to give the title product as white crystals (7.2 g, 71%).

5-(4-{[2-(Methylthio)pyrimidin-4-yl]oxy}phenyl)-N-[3-(trifluoromethyl) phenyl]-1,3,4-oxadiazol-2-amine. A 5-mL Emrys vial was charged with **3** (321 mg, 1.00 mmol) and anhydrous dioxane (5 mL). The vial was placed in a heating block at 100 °C. Solid cesium carbonate was added (326 mg, 1.0 mmol), followed after 10 min by 4-chloro-2-methylthiopyrimidine (177 mg, 1.10 mmol). The vial was then sealed and the reaction mixture was left to stir at 100 °C for 1 h. After cooling to ambient temperature, the reaction mixture was concentrated in vacuo. The residue was redissolved in DMF (5 mL), filtered through a 0.2-μm syringe filter, and purified by reverse-phase preparative HPLC. Fractions containing the product were combined and poured into EtOAc (50 mL). The resulting mixture was washed with saturated aqueous $NaHCO_3$ (2 × 50 mL) and brine (2 × 50 mL), dried over anhydrous Na_2SO_4, and filtered. Solvent was removed in vacuo to give the title product as a white solid (245 mg, 55%).

^{1}H NMR (500 MHz, DMSO-d_6): δ 2.36 (s, 3H), 6.89 (d, J = 5.8 Hz, ^{1}H), 7.37 (d, J = 7.9 Hz, ^{1}H), 7.48 (d, J = 8.8 Hz, 2H), 7.62 (t, J = 8.0 Hz, ^{1}H), 7.86 (dd, J = 8.3, 1.6 Hz, ^{1}H), 8.00 (d, J = 8.8 Hz, 2H), 8.10 (s, ^{1}H), 8.56 (d, J = 5.7 Hz, ^{1}H), 11.16 (s, ^{1}H). ^{13}C NMR (125 MHz, DMSO-d_6): δ 13.4, 103.8, 113.0, 118.1, 120.8, 121.1, 122.7, 124.1 (q, $J_{C\text{-}F}$ = 270.6 Hz, CF_3), 127.3, 129.8 (q, J = 31.5 Hz), 130.3, 139.4, 153.8, 157.5, 159.6, 159.7, 167.9, 171.4.

HRMS (ESI-TOF): calcd for $C_{20}H_{14}F_3N_5O_2S$ $[M+H]^+$ 446.0893, found 446.0885. Anal. Calcd for $C_{20}H_{14}F_3N_5O_2S$ x $0.5H_2O$: C, 52.86; H, 3.33; N, 15.41; S, 7.06. Found: C, 52.83; H, 3.06; N, 15.11; S, 7.03.

6-(4-(5-(3-(Trifluoromethyl)phenylamino)-1,3,4-oxadiazol-2-yl) phenoxy)pyrimidin-2,4-diamine (10). This compound was prepared according to the same procedure as in the synthesis of 5-(4-{[2-(methylthio)pyrimidin-4-yl]oxy}phenyl)-N-[3-(trifluoromethyl) phenyl]-1,3,4-oxadiazol-2-amine exemplified in Scheme 2.

^{1}H NMR (500 MHz, DMSO-d_6): δ 2.29 (s, 3H), 5.55 (s, ^{1}H), 6.97 (s, 2H), 7.36–7.39 (m, 3H), 7.62 (t, J = 8.0 Hz, ^{1}H), 7.83 (dd, J = 8.3, 1.6 Hz, ^{1}H), 7.95 (d, J = 8.8 Hz, 2H), 8.08 (s, ^{1}H), 11.11 (s, ^{1}H).

HRMS (ESI-TOF): calcd for $C_{20}H_{16}F_3N_6O_2S$ $[M+H]^+$ 461.1007, found 461.0996.

5-(4-{[6-Amino-2-(methylthio)pyrimidin-4-yl]oxy}phenyl)-N-[3-(trifluoromethyl)phenyl]-1,3,4-oxadiazol-2-amine (11). This compound was prepared according to the same procedure as in the synthesis of 5-(4-{[2-(methylthio)pyrimidin-4-yl]oxy}phenyl)-N-[3-(trifluoromethyl)phenyl]-1,3,4-oxadiazol-2-amine exemplified in Scheme 2.

^{1}H NMR (500 MHz, DMSO-d_6): δ 5.19 (s, ^{1}H), 6.04 (s, 2H), 6.33 (s, 2H), 7.28 (d, J = 8.7 Hz, 2H), 7.37 (d, J = 7.9 Hz, ^{1}H), 7.61 (t, J = 8.0 Hz, ^{1}H), 7.83 (dd, J = 8.0, 1.8 Hz, ^{1}H), 7.91 (d, J = 8.7 Hz, 2H), 8.08 (s, ^{1}H), 11.11 (s, ^{1}H).

HRMS (ESI-TOF): calcd for $C_{19}H_{15}F_3N_7O_2$ $[M+H]^+$ 430.1239, found 430.1229.

Compound Index (as appearing in order in the manuscript).

Compound 1

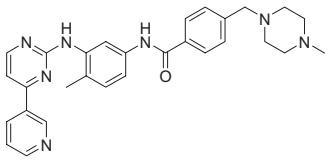

N-(3-(4-(pyridin-3-yl)pyrimidin-2-ylamino)-4-methylphenyl)-4-((4-methylpiperazin-1-yl)methyl)benzamide

Compound 2

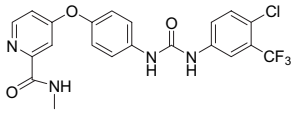

1-(4-(2-(methylcarbamoyl)pyridin-4-yloxy)phenyl)-3-(4-chloro-3-(trifluoromethyl)phenyl)urea

Compound 3

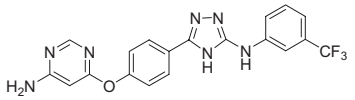

6-(4-(5-(3-(trifluoromethyl)phenylamino)-4*H*-1,2,4-triazol-3-yl)phenoxy)pyrimidin-4-amine

Compound 4

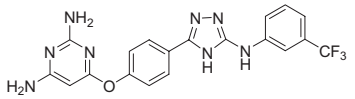

6-(4-(5-(3-(trifluoromethyl)phenylamino)-4*H*-1,2,4-triazol-3-yl)phenoxy)pyrimidine-2,4-diamine

Compound 5

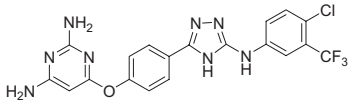

6-(4-(5-(4-chloro-3-(trifluoromethyl)phenylamino)-4*H*-1,2,4-triazol-3-yl)phenoxy)pyrimidine-2,4-diamine

Compound 6

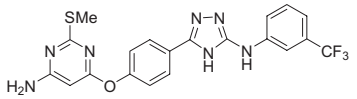

6-(4-(5-(3-(trifluoromethyl)phenylamino)-4*H*-1,2,4-triazol-3-yl)phenoxy)-2-(methylthio)pyrimidin-4-amine

Compound 7

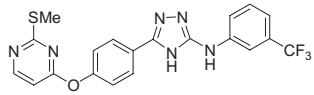

5-(4-(2-(methylthio)pyrimidin-4-yloxy)phenyl)-*N*-(3-(trifluoromethyl)phenyl)-4*H*-1,2,4-triazol-3-amine

Compound 8

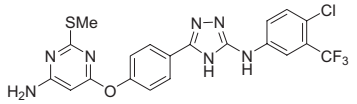

6-(4-(5-(4-chloro-3-(trifluoromethyl)phenylamino)-4*H*-1,2,4-triazol-3-yl)phenoxy)-2-(methylthio)pyrimidin-4-amine

Compound 9

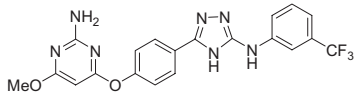

4-(4-(5-(3-(trifluoromethyl)phenylamino)-4*H*-1,2,4-triazol-3-yl)phenoxy)-6-methoxypyrimidin-2-amine

Compound 10

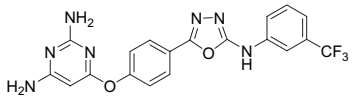

6-(4-(5-(3-(trifluoromethyl)phenylamino)-1,3,4-oxadiazol-2-yl)phenoxy)pyrimidine-2,4-diamine

Compound 11

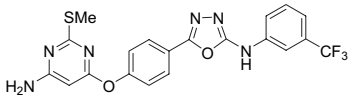

6-(4-(5-(3-(trifluoromethyl)phenylamino)-1,3,4-oxadiazol-2-yl)phenoxy)-2-(methylthio)pyrimidin-4-amine

Compound 12

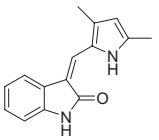

(*Z*)-3-((3,5-dimethyl-1*H*-pyrrol-2-yl)methylene)indolin-2-one

Compound 13

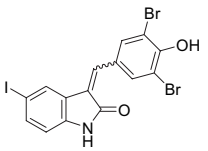

3-(3,5-dibromo-4-hydroxybenzylidene)-5-iodoindolin-2-one

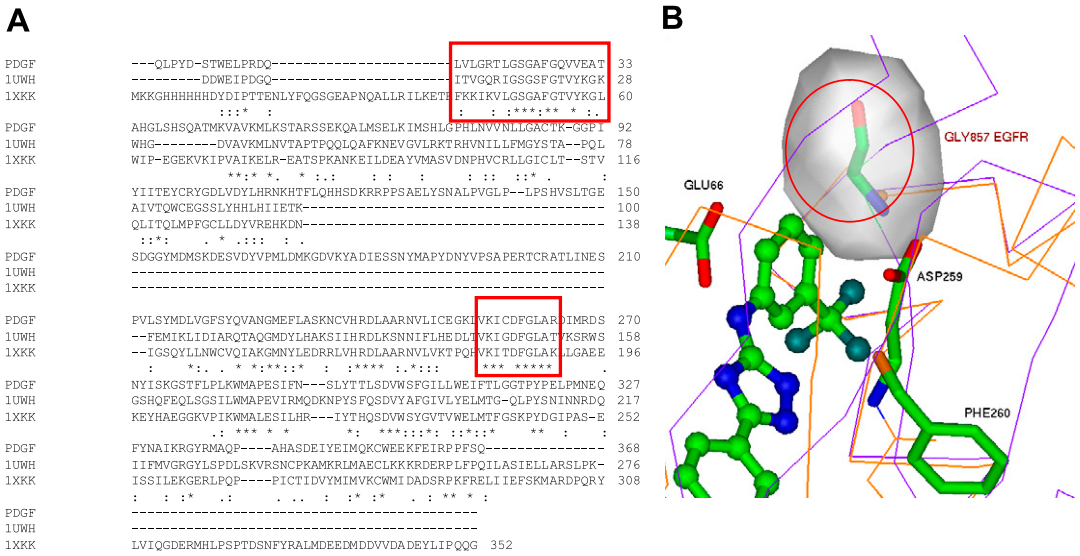

Fig. S1. Sequence alignment of EGFR, B-RAF, and PDGFRβ primary sequences and docking of **6** into PDGFRβ with an EGFR activation loop. (*A*) PDB ID code 1uwh represents the cocrystal structure of sorafenib with B-RAF, and PDB ID code 1xkk is the cocrystal structure of GW 572016 and EGFR. The sequence identity of the PDGFRβ and B-RAF kinase domains (if the insert LQHHSDKRRPPSAELYSNALPVGLPLPSHVSLTGESDGGYMDMSKDESVDYVPMLDMKGDVKYADIESSNY-MAPYDNYVPSAPERTCRATLINESPVL in PDGFRβ is excluded) is 29.1%, and overall similarity is 47.3% (opening gap penalty 15, extension gap penalty 1, using the program EMBOSS Align of the European Bioinformatics Institute [EMBL-EBI]). (*B*) Because of the absence of sufficient crystallographic information for the activation loop in PDGFRβ, it can be modeled with a variety of possible loop conformations. By modeling the conformation of the activation loop in PDGFRβ near Gly857 using EGFR kinase (PDB ID code 1xkk) as a template, we observe that Gly857 will be located in close proximity to the phenyl ring of **6**. Further addition of any atoms in the *para* position would be sterically hindered by the loop. This would be predicted to create an unstable position of **6** in the protein and potentially explains why 4-Cl is not tolerated for PDGFRβ activity. Orange, PDGFR; violet, EGFR.

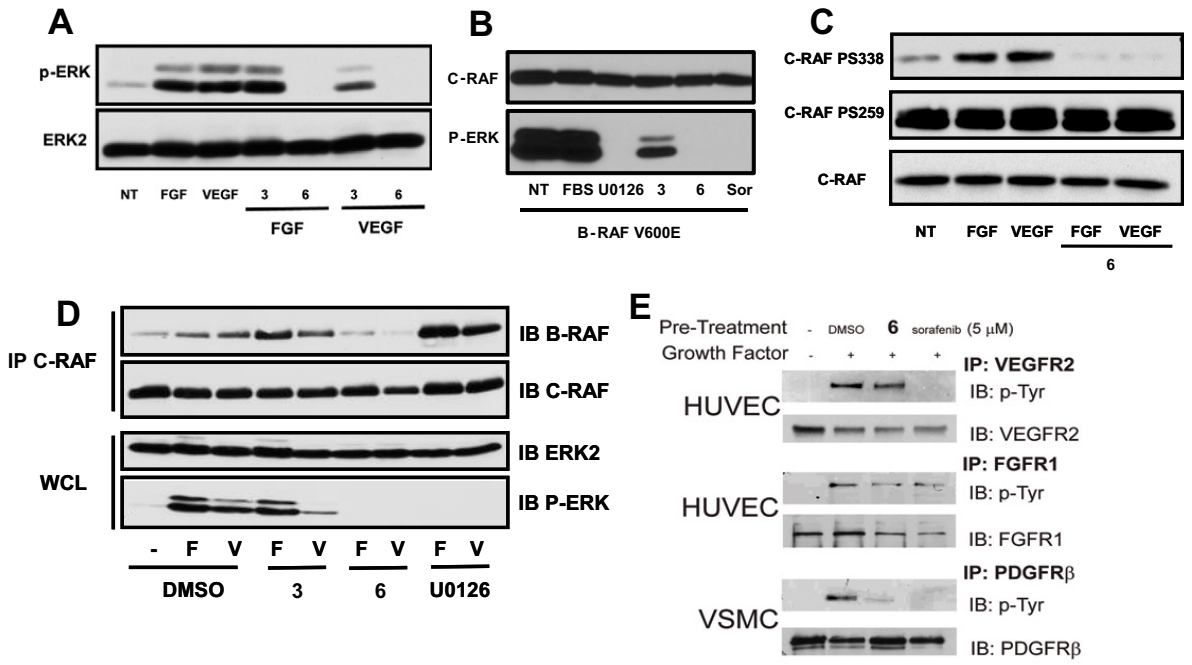

Fig. S2. Compound **6** inhibits RAF activity in ECs, active B-RAF V600E, phosphorylation of C-RAF S338, and heterodimerization of B-RAF/C-RAF without affecting FGFR or VEGFR. (*A*) Western analysis comparing **3** and **6** (10 μM) inhibition of bFGF or VEGF (50 ng/ml, 5-min stimulation) induced phosphorylation of ERK in serum-starved HUVECs as described in *SI Materials and Methods*. ERK2 staining is shown for the loading control. (*B*) 1205Lu melanoma cells, which endogenously express constitutively active B-RAF V600E, were starved overnight and treated for 1 h with **6** (10 μM) to determine inhibition of the oncogenic B-RAF activity as measured by phosphorylation of ERK. (*C*) Phosphorylation of C-RAF within the activation segment at S338 or at the 14-3-3 binding site, S259, was determined by western analysis. Endothelial cells were serum-starved overnight and pretreated with compound **6** for 1 h before stimulation with either bFGF or VEGF at 50 ng/ml for 5 min. (*D*) Immunoprecipitation and western analysis of B-RAF/C-RAF heterodimerization. HUVECs were serum-starved overnight and treated with compounds as described in *C* above. After growth-factor stimulation with bFGF (F) or VEGF (V), C-RAF was immunoprecipitated (agarose-conjugated C-RAF Ab; Santa Cruz Biotechnology) from 400 μg of protein from total cell lysates, and the presence of B-RAF (Santa Cruz Biotechnology) in the immunoprecipitate was determined by western blotting. Corresponding phosphorylation of ERK in the whole-cell lysates (WCL) is shown in the bottom panel. Total ERK2 and total C-RAF were included in the blots as loading controls. (*E*) Human umbilical vein endothelial cells (HUVECs) or human vascular smooth muscle cells (VSMCs) were pretreated with DMSO, **6**, or sorafenib for 1 h followed by 5-min stimulation with growth factor and lysis in RIPA buffer. Five hundred micrograms of protein was incubated with 3 μg of antibody (sc-432 for PDGFRβ and sc-6251 Flk-1/KDR, both from Santa Cruz Biotechnology; and 05-149 from Upstate Biotechnology for FGFR1) for 1 h at 4 °C before the addition of Protein A/G Plus agarose beads (Santa Cruz Biotechnology). To measure autophosphorylation, immunoblots were carried out with a phospho-tyrosine antibody (PY-20; Santa Cruz Biotechnology) for 1 h and detected with chemiluminescence. Membranes were stripped and reprobed for total receptor levels of PDGFRβ, Flk-1/KDR, and FGFR1, respectively (sc-339 and sc-504, and 05-149, from Santa Cruz Biotechnology and Upstate Biotechnology, respectively).

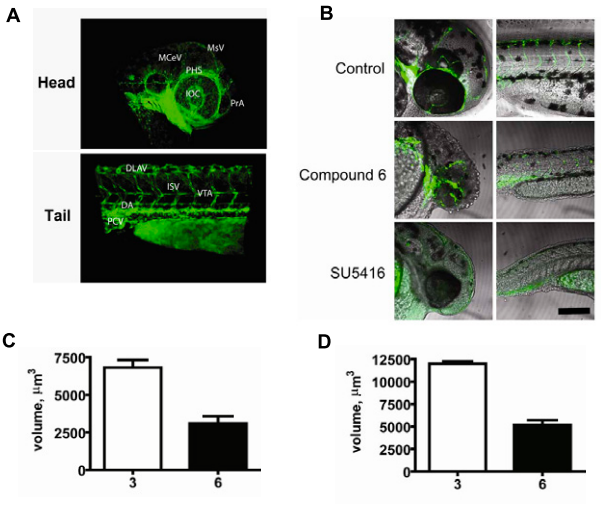

Fig. S3. Labeling of the Tg:*fli1-egfp* zebrafish vasculature and quantification of the drug treatment effect on the intersegmental vessel volume. (*A*) Images are taken from Fig. 3*A* with major vascular structures labeled. In the head: MCeV, middle cerebral vein; MsV, mesencephalic vein; PHS, primary head sinus; IOC, inner optic circle; PrA, prosencephalic artery. In the tail: DLAV, dorsal longitudinal anastomotic vessel; DA, dorsal aorta; PCV, posterior cardinal vein; ISV, intersegmental vessel; VTA, vertebral artery. (*B*) Representative views of zebrafish embryos treated as in Fig. 3*A* (images represent merged phase and GFP fluorescence views of the head and trunk regions of *Tg:fli1-EGFP* embryos). (Scale bar, 200 μm.) (*C*) Quantification of ISV volume from embryos treated as in Fig. 3*A*. (*D*) Quantification of ISV volume from embryos treated as in Fig. 3*B*. To measure the ISV volume, individual ISVs were digitally isolated using the Imaris countersurface/isosurface functions. Thirty independent ISVs from four independent embryos were used for the measurement. Reported ± SEM.

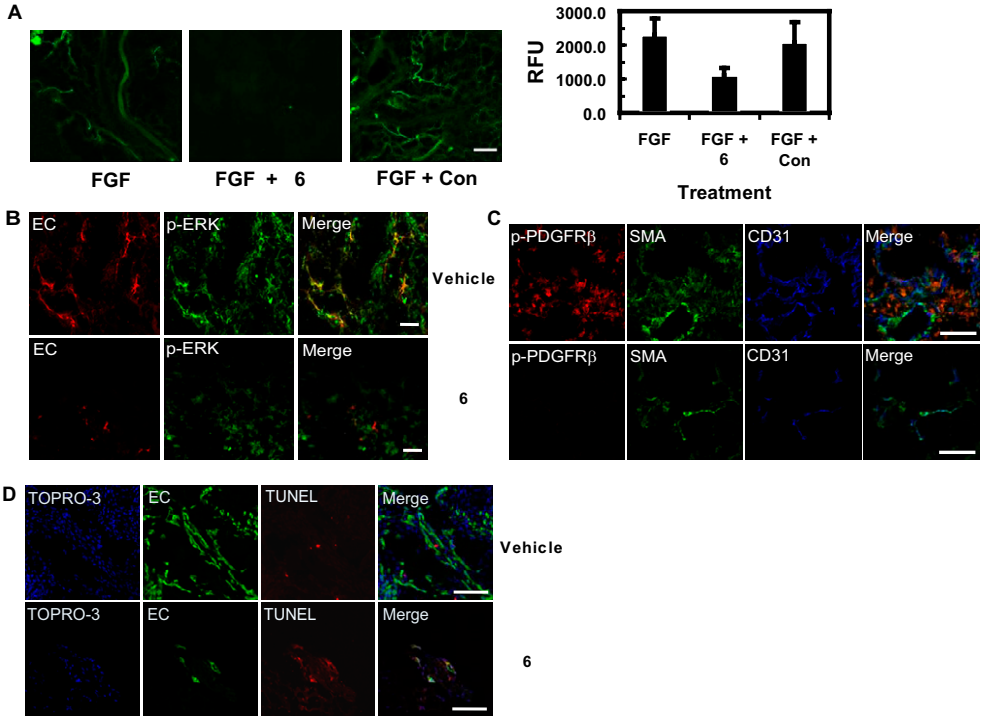

Fig. S4. Compound **6** disrupts angiogenesis in mice. (*A*) **6** inhibits bFGF-induced angiogenesis in the mouse Matrigel model. Mice (n = 5) were injected in the flank with growth-factor-depleted Matrigel loaded with 200 ng bFGF and treated for 5 days with 50 mg/kg **6** via i.p. administration twice daily (bid). On day 5 after implantation of the Matrigel, mice were administered FITC-lectin to label blood vessels. The plugs were removed and visualized by confocal microscopy followed by homogenization and quantification of total FITC. Error bars represent ± SEM. (*B*) **6** inhibits phosphorylation of ERK in blood vessels. Thin sections (5-μm) of the Matrigel plugs were immunostained for vessels with an EC mix (anti-Flk, anti-CD31, anti-VE-cadherin, and anti-endoglin). Matrigel sections were immunostained for phospho-ERK to detect in vivo inhibitory activity of **6** by confocal microscopy. (*C*) **6** inhibits phosphorylation of PDGFRβ Y751 in stromal cells. Thin sections (5-μm) of the Matrigel plugs were immunostained for pericytes and fibroblasts with α-smooth muscle actin and for phospho-PDGFRβ Y751 levels. ECs were immunostained with anti-CD31. (*D*) **6** induces apoptosis in the endothelium but not in the surrounding stromal cells in the Matrigel plugs. Thin sections (5-μm) of the Matrigel plugs were immunostained for vessels with an EC mix (described as in *B*). TO-PRO-3 was used as a nuclear counterstain and TUNEL staining was used to detect apoptotic nuclei. Images were taken using confocal laser-scanning microscopy (n = 4 plugs/group in *B*–*D*). [Scale bars, 200 μm (*A*, *C*, *D*); 100 μm (*B*).]

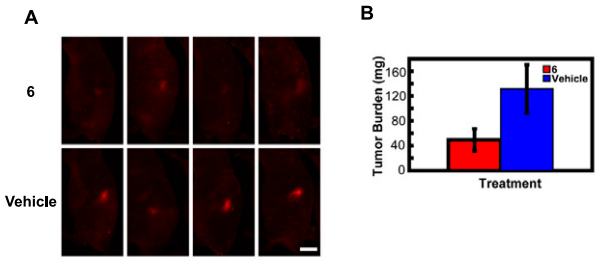

Fig. S5. Compound **6** is orally active against orthotopic renal cell carcinoma. (*A*) Real-time fluorescent imaging of SN12C-RFP renal cells orthotopically injected into the kidneys of nu/nu mice. Mice were treated with either vehicle or **6** (100 mg/kg, po, qd). Drug treatments were started 7 days after orthotopic injection, and tumor growth was visualized every 7 days by whole-animal imaging. The images shown are of 4 mice in the vehicle- and drug-treated groups on day 26. (Scale bar = 10 mm.) (*B*) At the end of the study, both the left tumor-bearing kidney and right kidney were extracted and weighed. The graph shows the mean difference in weight between the tumor-bearing kidney and the normal kidney in each animal. n = 6 animals/group. *P = 0.05.

Table S1. In vitro kinase panel comparing 3, 6, and sorafenib

	Inhibition at 10 μM (%)		
Kinase target	Cmp **3**	Cmp **6**	Sorafenib
ABL1	4	3	50
AKT1	1	2	2
B-RAF	17	−1	84
CDK2	2	2	2
CSF1R	79	23	101
CK2 alpha 1	−3	0	−3
EGFR	−2	−3	−3
EGFR L858R	−3	−10	−5
EGFR L861Q	−1	−4	−4
FGFR1	9	6	44
FGFR2	−1	−2	83
FGFR3	−12	−13	37
FGFR3 K650E	4	−1	78
FGFR4	−6	−7	7
FLT1 (VEGFR1)	5	−2	93
FLT3	−4	−2	9
FLT3 D835Y	29	9	72
IGF1R	−4	0	−3
KDR (VEGFR2)	31	16	104
KIT	74	28	37
MEK1	−5	−2	0
MEK2	−8	−6	−4
ERK2	−4	−5	0
JNK3	−8	−8	−4
ERK1	1	2	3
JNK1	−5	−3	−2
JNK2	−7	−4	10
MAPKAPK2	1	2	2
MET (cMet)	7	3	2
MET M1250T	4	−1	3
PAK2	2	1	2
PDGFR beta	35	20	93
PKC alpha	−5	−1	−2
PKC beta I	−3	2	−1
PKC beta II	−3	−4	−3
PKC delta	−1	−1	−4
PKC epsilon	−3	−1	−2
PKC gamma	6	5	−3
PKC eta	1	3	2
PKC iota	−2	0	−2
FAK2	−4	−4	−3
CRAF Y340D Y341D	38	3	95

Table S2. Kinases screened with 10 μM 6 in the KINOME*scan* profiling assay at Ambit Biosciences used to construct Fig. 2

Kinase	% Control
ABL1	100
AMPK-alpha1	72
ARK5	70
AXL	87
BMX	97
B-RAF	91
B-RAF(V600E)	98
CDC2L1	70
CDC2L2	83
CDK11	32
CDK11	32
CDK2	87
CDK3	91
CDK5	88
CDK7	97
CDK8	67
CDK9	100
CLK2	84
CSF1R	51
CSNK1E	47
DYRK1B	85
EPHA2	100
EPHB4	94
ERK2	90
FAK	100
FGFR2	100
FLT1	81
FLT3	2.8
FLT3(D835H)	17
FLT3(D835Y)	18
FLT3(ITD)	3.1
FLT3(N841I)	3.1
FLT4	100
GSK3B	90
IGF1R	100
INSR	100
JNK1	98
KIT	0
KIT(D816V)	76
KIT(V559D)	0.1
KIT(V559D,T670I)	56
KIT(V559D,V654A)	15
LIMK2	72
LKB1	100
MEK1	84
MET	94
MLK3	96
MYO3A	94
p38-alpha	100
PAK1	100
PAK4	100
PDGFRA	0.25
PDGFRB	0.5
PFTK1	71
PIK3CA	100
PIM1	96
PKAC-alpha	100
PRKCD	74
PRKCE	91
PRKD1	100
RAF1	52
RET	95

Table S2. (Continued)

Kinase	% Control
RIOK3	100
RIPK1	84
SRC	90
SRPK2	100
TIE1	76
TIE2	88
TRKA	64
VEGFR2	80

Table S3. Kinome profile of 6 in the competitive binding assay (KINOME*scan*; Ambit Biosciences)

Kinase	K_d (nM)
FLT3	52
KIT	170
PDGFRα	300
PDGFRβ	520
CDKL2	5,100
CDK11	7,500
ABL	>10,000
B-RAF	>10,000
CSF1R	>10,000
FGFR2	>10,000
p38α	>10,000
PAK1	>10,000
RET	>10,000
VEGFR2	>10,000

Eleven-point K_ds were determined for targets which demonstrated inhibition at 10 μM shown in Fig. 2.

Table S4. Cell-based profiling of 6. HUVECs were pretreated with 6 for 1 h and stimulated with bFGF for 5 min. For PDGFRβ, VSMCs were pretreated with 6 for 1 h and stimulated with PDGF-BB for 7 min, because HUVECs do not express this receptor

Phospho-protein	Inhibition
C-RAF S259	–
C-RAF S621	–
C-RAF S338	+
MEK-1/2 S217/S221	+
ERK-1/2 T202/Y204	+
ERK-5 T218/Y220	–
Bad S112 or S155	–
Src Y416	–
Pan phospho-PKC	–
p38 T180/Y182	–
SAPK T183/Y185	–
FAK Y861	–
Akt S473	–
VEGFR2 (phospho-tyrosine)	–
FGFR1 (phospho-tyrosine)	–
PDGFRβ (phospho-tyrosine) in SMCs	+